(Preprint) AAS 17-269

ORBIT MAINTENANCE AND NAVIGATION OF HUMAN SPACECRAFT AT CISLUNAR NEAR RECTILINEAR HALO ORBITS

Diane Davis [*], Sagar Bhatt [†], Kathleen Howell [‡], Jiann-Woei Jang [†], Ryan Whitley [§], Fred Clark [†], Davide Guzzetti [¶], Emily Zimovan [‖], and Gregg Barton [†]

Multiple studies have concluded that Earth-Moon libration point orbits are attractive candidates for staging operations. The Near Rectilinear Halo Orbit (NRHO), a member of the Earth-Moon halo orbit family, has been singularly demonstrated to meet multi-mission architectural constraints. In this paper, the challenges associated with operating human spacecraft in the NRHO are evaluated. Navigation accuracies and human vehicle process noise effects are applied to various stationkeeping strategies in order to obtain a reliable orbit maintenance algorithm. Additionally, the ability to absorb missed burns, construct phasing maneuvers to avoid eclipses and conduct rendezvous and proximity operations are examined.

INTRODUCTION

To further human space exploration in a stepwise approach, orbit characterization studies have endeavored to evaluate potential locations in cislunar space that are favorable for meeting common human exploration objectives. In that vein, the Near Rectilinear Halo Orbit (NRHO) has been demonstrated as a staging orbit favorable for missions both to the surface of the Moon and for departure to deeper space destinations.[1] While a growing number of robotic missions have completed successful operations to various types of specific libration point orbits,[2,3] human missions have never been conducted to orbits of this particular class. In addition, neither robotic nor human missions have been operated in the NRHO regime specifically, and NRHOs exhibit dynamical characteristics that are unique in comparison to all other libration point orbits. Like other multi-body orbits, the periodic characteristics of the NRHOs cannot be effectively characterized within the classical two-body orbit dynamics framework more familiar to the human spaceflight community.[4–7] In fact, a given NRHO is not easily identified by simply specifying Keplerian orbit parameters, and a valid specific epoch state vector must be first obtained through iteration in a multibody dynamical model.

In this paper, the dynamical sensitivity of the NRHO is fully characterized along with the projected propulsive costs of conducting human missions in the multi-body regime. First, navigation accuracies and human vehicle process noise effects are identified and applied to a valid NRHO state to assess the perturbation of the orbit due to these disturbances. Second, the ability to maintain the orbit over the lifetime of a habitat mission by applying a reliable orbit maintenance strategy is investigated. The NRHO, while similar in some ways to the quasi-halo orbits from the ARTEMIS mission,[8] requires an updated orbit maintenance strategy. Such a reassessment is due to several dynamical differences such as the relative stability of the NRHO as compared to many other halo orbits and the close passage over the lunar surface. Third, current navigation accuracies and process noise parameters are evaluated against proposed orbit maintenance strategies through Monte Carlo and LINCOV (linear covariance) uncertainty analysis. Sensitivity to various types and levels of

[*] Principal Systems Engineer, a.i. solutions, Houston, TX, 77058
[†] Aerospace Engineer, Draper, Houston, TX, 77058
[‡] Hsu Lo Distinguished Professor of Aeronautics and Astronautics, School of Aeronautics and Astronautics, Purdue University, 701 West Stadium Avenue, West Lafayette, IN 47907-2045
[§] Aerospace Engineer, Exploration Mission Planning Office, NASA JSC, Houston, TX, 77058
[¶] Ph.D. Candidate, School of Aeronautics and Astronautics, Purdue University, 701 West Stadium Avenue, West Lafayette, IN 47907-2045
[‖] Graduate Student, School of Aeronautics and Astronautics, Purdue University, 701 West Stadium Avenue, West Lafayette, IN 47907-2045

uncertainties allow navigation requirements to be correlated with a comparable stationkeeping propellant Δv budget. Both navigation error and process noise disturbance forces can be significant drivers for orbit maintenance costs. Fourth, the ability to handle off-nominal situations such as missed burns and phasing maneuvers to avoid eclipses are examined. As the NRHO is mostly out of the Earth-moon plane, the costs to avoid long eclipses are minimal. Finally, rendezvous and proximity operations are vital aspects of multi-mission human exploration endeavors. The ability to conduct rendezvous and the associated propellant costs are assessed as well as the impacts of various profile assumptions including the location within the NRHO the rendezvous is performed. The results of these studies will determine the feasibility of operating and maintaining long term human assets in NRHOs.

THE L_2 HALO FAMILY AND SELECTED NRHOS

Near Rectilinear Halo Orbits (NRHOs) are members of the halo families of orbits in the vicinity of the collinear libration points.[5] Perfectly periodic in the Circular Restricted 3-Body (CR3B) model, halo orbits bifurcate from in-plane Lyapunov orbits around the libration points. The halo orbits expand out-of-plane until they are nearly polar. These out-of-plane members of the halo families, with the close approach distance relative to the smaller primary decreasing, comprise the NRHOs. In the Earth-Moon system, the L_1 and L_2 halo families evolve out of the Earth-Moon plane, with NRHOs approaching the Moon. The L_2 southern Earth-Moon halo family appears in Figure 1(a), with two NRHOs highlighted in white. The L_1 and L_2 northern and southern NRHOs appear in Figure 1(b).

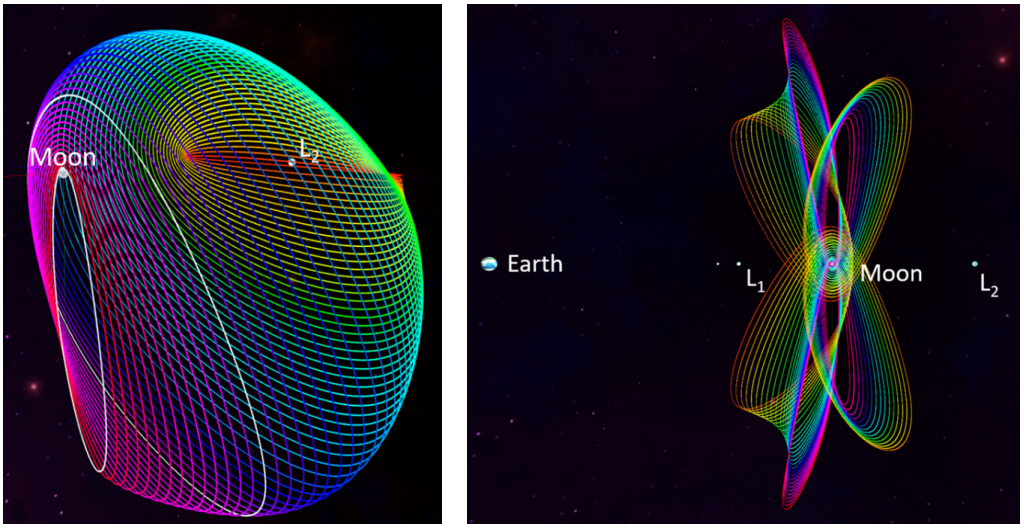

(a) L_2 southern halo family (b) L_1 and L_2 northern and southern NRHOs

Figure 1: Earth-Moon halo orbits

The stability characteristics of the halo families can be used to define the boundaries of the NRHO portions of the halo families. The stability index[6] ν is a function of the maximum eigenvalue of the monodromy matrix, i.e., the state transition matrix (STM) of the halo orbit after precisely one revolution. The stability index is evaluated as

$$\nu = \frac{1}{2}\left(\lambda_{max} + \frac{1}{\lambda_{max}}\right) \tag{1}$$

A halo orbit characterized by a stability index equal to one is considered marginally stable from a linear analysis. A stability index greater than one corresponds to an unstable halo orbit; the higher the value of ν, the faster a perturbed halo orbit will tend to depart its nominal path. An image of the L_1 and L_2 halo family stability indices, plotted against perilune radius, appears in Figure 2(a). The unstable, nearly-planar halo orbits exist at the far right of the plot, characterized by high stability indices and large perilune distances. As the

halo families evolve out of plane, their stability indices decrease as the periapsis approaches the Moon and the linear instability decreases. The Earth-Moon L_1 and L_2 NRHOs possess single-digit linear stability indices. A zoomed-in plot of the NRHO stability indices appears in Figure 2(b). At very small perilune radii, the halo orbits are marginally stable from the linear analysis. As r_p increases, the stability characteristics change (at $r_p \approx 1{,}850$ km for the L_2 family) and the orbits become very slightly unstable. As r_p continues to increase, the stability characteristics change again (at $r_p \approx 13{,}500$ km for the L_2 family), and the halo families return to marginal stability in the linear sense. Continuing to move to the right in Figure 2(b), perilune distance increases until yet another stability change occurs (at $r_p \approx 17{,}350$ km for the L_2 family). After this point, the halo orbits quickly become increasingly unstable. Within each halo family, the NRHOs can be defined according to these linear stability properties. The NRHO portion of the halo families can be bounded by the bifurcating orbits in with in Figure 1(b). For the Earth-Moon system, the perilune radii of the NRHOs range from $r_p \approx 1{,}850$ to $r_p \approx 17{,}350$ and all are accessible.

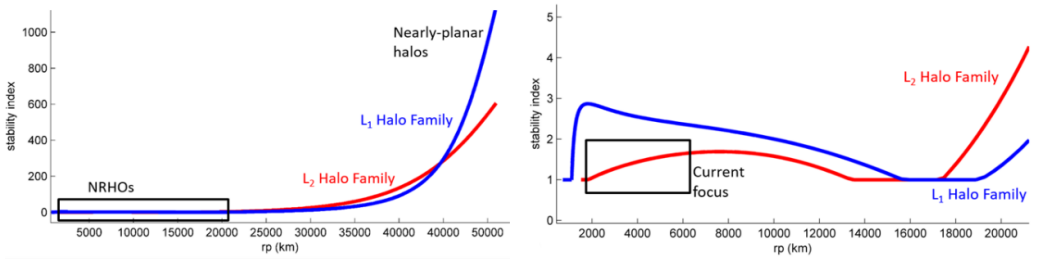

(a) L_1 and L_2 halo family stability indices

(b) L_1 and L_2 NRHO stability indices

Figure 2: Earth-Moon L_1 (blue) and L_2 (red) halo stability indices

The current investigation focuses on L_2 Southern NRHOs with perilune radii between 2,100 and 6,500 km. Perfectly periodic in the CR3B model, the NRHOs retain many of their characteristics in a higher-fidelity force model and exist as quasi-periodic orbits that offer advantages for cislunar exploration. Each higher-fidelity NRHO is labeled consistent with the perilune radius of its corresponding CR3B periodic NRHO. Several orbits are of particular interest. A 2100 km r_p NRHO is attractive due to low stationkeeping costs. A slightly higher NRHO with $r_p \approx 3233$ km is in a 9:2 resonance with the lunar synodic cycle. It can, thus, be oriented to avoid eclipsing due to the Earth. An NRHO with a perilune distance of 4500 km is in a 4:1 sidereal resonance with the Earth. Finally, a 5930 km NRHO is in a 4:1 resonance with the lunar synodic cycle, and, while its orbital parameters can vary more than the others, this NRHO can also be oriented to avoid all eclipses from both the Earth and the Moon for extended periods.[9] For completeness, several other reference NRHOs are also examined.

NRHO NAVIGATION ASSESSMENT

A critical component of mission success is accurate knowledge of the spacecraft state. It is assumed the spacecraft rotational state can be determined using onboard sensors such as star trackers or Sun sensors. The focus of this paper is on the spacecraft translational state (position and velocity) needed for orbit maintenance. With the exception of proximity operations (discussed later) when relative sensors can be used, the primary means of spacecraft navigation in cislunar space relies on ground-based tracking stations such as the NASA Deep Space Network (DSN). The orbit is determined on the ground and sent to the spacecraft to update the onboard state. Communication with the spacecraft is determined by mission event schedule, orbit geometry, and network access. An autonomous navigation system is likely desired as backup in the event ground updates are unavailable. One approach is to place a constellation of satellites and/or ground beacons at the Moon to which radiometric measurements can be taken. An alternative that does not require supporting infrastructure is taking optical measurements of the Moon,[10] which is an approach NASA may use and is presented here.

Linear Covariance Analysis

To assess navigation performance quickly, linear covariance analysis is used.[10–12] Linear covariance (LinCov) analysis is a methodology to obtain navigation and trajectory dispersion statistical performance characteristics in a single simulation run. It is based on linearization about a pre-defined (nonlinear) nominal trajectory and propagation and updating of covariance matrices. It can provide a top-level analysis of a closed-loop guidance, navigation, and control system useful in deriving requirements before higher-fidelity simulations are available. As such, it is a great complement to Monte Carlo analysis.

Two common metrics to characterize overall system and navigation performance are trajectory dispersions and navigation errors. Trajectory dispersions are defined as the difference between the true (actual) state and the nominal (desired or reference) state. The covariance of the trajectory dispersions indicates how precisely the system can follow a desired trajectory. The navigation error is the difference between the true and navigation (estimated) states. The covariance of the navigation error characterizes how precisely the onboard navigation system can determine the true state.

A common approach to obtain these performance metrics is to use a Monte Carlo simulation, where the sample statistics of hundreds or thousands of runs are used to numerically compute the desired covariance matrices. This statistical information can be obtained using linear covariance analysis techniques by directly propagating, updating, and correcting an augmented state covariance matrix.

NRHO Dynamics and Navigation Options

Trajectory dispersions generated with LinCov provide insight into the properties of NRHOs. In modeling the dynamics, a higher-fidelity, ephemeris-based, multi-body gravity model is used with spherical harmonics for the Moon. Other disturbances, such as solar radiation pressure (SRP), are not modeled explicitly but treated as process noise during covariance propagation. For a spacecraft inhabited by humans, the expulsion of waste water and CO_2 as well as imperfect attitude control also impart a force on the spacecraft. Thus, in this paper, urine dumps, pressure swing adsorption (PSA) puffs, attitude deadbanding, and attitude slews are all considered in the process noise. Table 4 lists the sources and magnitudes of the process noise used in LinCov analyses.

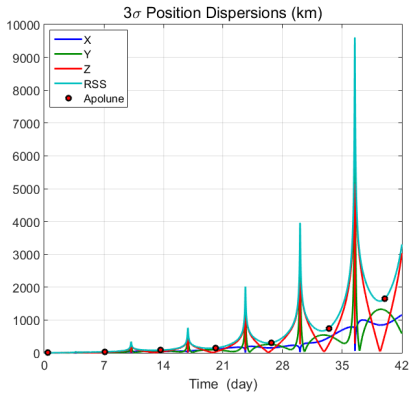

Figure 3: Position dispersions for a ballistic NRHO trajectory.

As an example, Figure 3 shows position dispersions for the $r_p \approx 3233$ km NRHO with an initial epoch of 09 Jan 2020 in the moon-centered rotating (MCR) frame. The mean period of one revolution for this NRHO is approximately 6.6 days, and the time of each apolune is indicated with red dots. In this case, the dispersions increase from an initial 3σ value of 1 km to thousands of km in 6 revolutions, emphasizing the need for stationkeeping. The pattern of dispersions rapidly increasing to a peak near perilune then abating until around apolune is typical for the NRHOs in this paper. The close approach to the Moon results in fast dynamics during which any difference between nominal and perturbed trajectories would be magnified. Consequently, it is preferred to avoid stationkeeping maneuvers near perilune.

With initial navigation error magnitudes of 1 km and 1 cm/s (3σ), the navigation error would grow similarly to the trajectory dispersions in Figure 3 if no measurements or ground updates were provided. At a minimum, a good estimate of the spacecraft state is required when computing Δv for stationkeeping maneuvers (e.g., every apolune). In Figure 4, a ground update with an accuracy of 1 km, 1 cm/s (3σ) is performed at every apolune. The blue dots at the top of the figure indicate when an update takes place. Although the navigation errors still grow fairly large between updates, it is not a concern as long as stationkeeping maneuvers are not

performed in that interval.

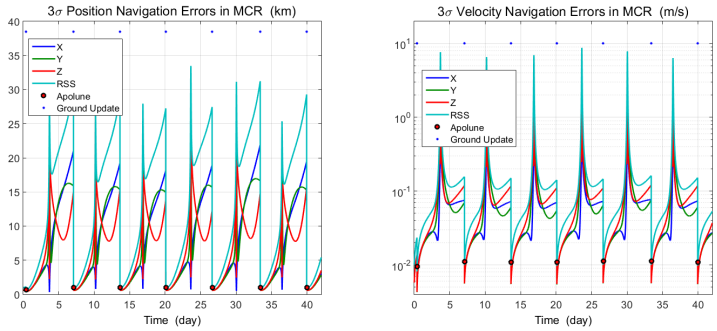

Figure 4: Position and velocity navigation errors with ground updates at every apolune.

Without ground updates, an optical navigation technique could be used in which an image of the Moon taken by a camera is processed to compute the centroid and apparent diameter of the Moon. Then the spacecraft position can be calculated using the known diameter and inertial position of the Moon. It is assumed that the camera can be oriented to place the Moon in its field of view when a measurement is needed, either by gimbaling the camera or slewing the spacecraft. The camera has a resolution of 2592 x 1944 pixels and focal length is 16 mm. Error values (1σ) for noise and bias are 1/3 pixel and 1/15 pixel, and camera misalignment (1σ) of 15 arcsec and camera position offset of 0.1 m are assumed. Figure 5 illustrates optical navigation performance.

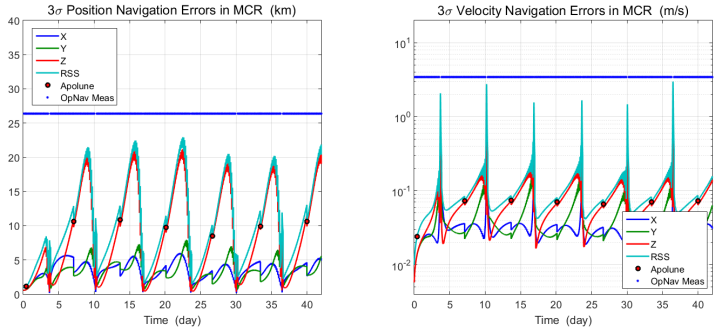

Figure 5: Position and velocity navigation errors with optical measurements every 3 hours.

Measurements are taken over a 60-second interval every 3 hours, as indicated by the blue dots at the top of the figure. Navigation error magnitudes of less than 11 km and 7.5 cm/s (3σ) can be achieved near apolune. Even better navigation performance is possible near perilune since the measurements improve as the Moon gets closer (as long as the full disk of the Moon can be captured in the field of view). With state estimates provided using optical navigation, one of the orbit maintenance methods described in the next section can be used to perform stationkeeping, an example of which is given in Figure 6.

Navigation performance improvements can be achieved by careful investigation and selection of the camera specifications, measurement frequency, and duration of the optical navigation passes. The ability to generate low navigation error magnitudes demonstrate that optical navigation is a viable backup to ground updates.

NRHO ORBIT MAINTENANCE METHODS

The key to maintaining assets in NRHOs pivots on the ability to stationkeep. Multiple strategies for stationkeeping libration point orbits have been previously investigated; overviews of various methods appear in Folta et al.[13] and Guzzetti et al.[14] Two particular strategies for NRHO orbit maintenance are examined in the current analysis: x-axis crossing control and Cauchy-Green Tensor (CGT) targeting. The stationkeeping analysis is framed to support three objectives to assess the feasibility of an NRHO as a baseline concept:

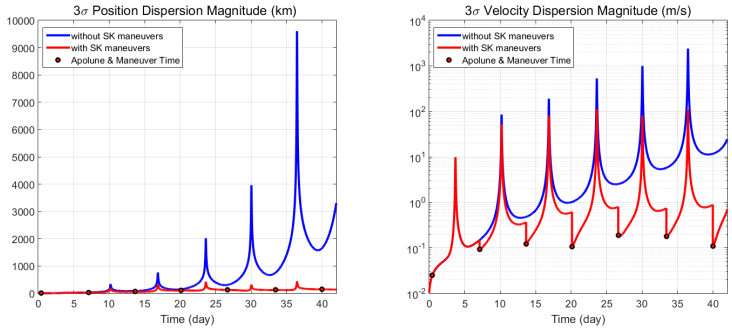

Figure 6: Stationkeeping maneuvers every rev using optical navigation.

1. Determine a long-term reference path. Such a trajectory can be constructed as a true baseline or as a virtual reference during different phases of the mission. The long-horizon reference may require infrequent maneuvers and updates to accommodate significant events such as eclipse avoidance, missed burns, and other anomalies.
2. Deliver bounds for maintenance requirements to offset perturbations to the path. Such perturbations include navigation errors and maneuver execution errors. In addition, the impact of spacecraft errors are examined, including attitude deadbanding and slew errors and human spaceflight-related forces such as CO_2 expulsion and urine dumps. Two short-horizon stationkeeping strategies are included to gain insight into the dynamics and vehicle response to errors: CGT targeting and x-axis crossing control.
3. Assess the impact of off-nominal events, e.g., missed stationkeeping maneuvers and phasing maneuvers to avoid eclipse or enable rendezvous.

Long-Horizon (LH) Reference Orbit Generation

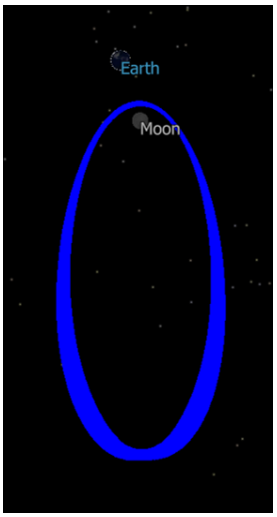

Figure 7: Earth-Moon Southern L_2 NRHO in a higher-fidelity force model for 500 revolutions

Both the CGT targeting and the x-axis crossing control methods can simultaneously meet the long-horizon and short-horizon challenges in a single step. However, it is computationally advantageous to separate the two regimes of orbit maintenance. Thus, a long-horizon reference is created as the first step in a two-step stationkeeping process.[9,14] A periodic NRHO in the CR3B model acts as an initial guess for a quasi-periodic halo in the higher-fidelity force model. Node points, or patch points, from the periodic halo orbit are input into a differential corrections process to construct a continuous, quasi-periodic trajectory in the ephemeris force model. Multiple methods are available for this corrections process. In the current study several methods are implemented, including multiple shooting[14] and forward/backward shooting via the sparse solver SNOPT.[9] These two methods are implemented for creating reference NRHOs with durations of 20-100 revolutions. A third procedure uses a receding-horizon approach[9,15] and targets a rotating x-velocity (v_x) equal to 0 many revolutions downstream to extend an existing reference orbit for 500 revolutions (˜9-10 years) or more. A 500-revolution 9:2 synodic NRHO ($r_p \approx 3233$ km) in a higher-fidelity force model appears in Figure 7. All three approaches are valid and none emerged as consistently superior to the others.

Long-term reference trajectories generated by these three schemes are essentially continuous, that is, discontinuities in the orbits are small relative to noise and errors involved in the stationkeeping process, and the trajectories can effectively act as reference orbits for orbit maintenance. For example, the total Δv corresponding to the sum of the discontinuities in the long-term reference orbit pictured in Figure 7 is less than 28 mm/s per year. It is noted that larger discontinuities along the reference path can lead to larger stationkeeping costs; maintaining a non-ballistic trajectory is more expensive. If stationkeeping to a reference orbit, it is

important that the reference be effectively ballistically continuous to maintain low stationkeeping costs. The reference generation process results in a long-horizon orbit that accommodates the dynamics of a higher-fidelity force model including multiple gravitational bodies and spherical harmonics. This reference orbit supplies a target for short-horizon orbit maintenance. Note that the reference can be virtual and updated as necessary.

Short-Horizon (SH) Orbit Maintenance

An NRHO is either marginally stable in a linear sense or nearly so; while it is more robust to perturbations than an unstable halo orbit nearer the L_1 or L_2 libration points, it remains sensitive to variations. When the initial state from a converged reference NRHO is propagated forward in time without introducing navigation or spacecraft errors, it will escape from the vicinity of the Moon in a finite time due to the buildup of numerical integration errors or slight model differences. When navigation and spacecraft errors are included in the simulation, the time to escape shortens, and the spacecraft can depart the vicinity of the Moon within 5-15 revolutions. To remain in an NRHO long term, an orbit maintenance scheme is required; regularly scheduled maneuvers can maintain the orbit as is necessary, for example, to support a long-term habitat. Two strategies are examined for NRHO orbit maintenance: x-axis crossing control and CGT targeting.

X-Axis Crossing Control An x-axis crossing control strategy applies a maneuver to target a user-defined set of constraints at a future location along the orbit. Similar methods have been successfully applied for halo orbiters at Earth-Moon and Sun-Earth libration points, including ARTEMIS[3,13] and WIND.[16] In the current analysis, an x-axis crossing control strategy is adapted to the different characteristics of the NRHO as compared to previously-flown spacecraft placed in halo orbits: increased orbital stability, decreased orbital period, and closer approaches to the Moon. However, an effective strategy for NRHO stationkeeping depends on many variables, including maneuver placement and selection of target constraints and locations.

Maneuver Placement. The orbit maintenance costs associated with an x-axis crossing algorithm depend on the frequency and location of short-horizon (SH) maneuvers throughout the NRHO. While previously flown libration point orbiters have planned multiple maneuvers per revolution, for an NRHO with perilune radius between 2100 and 6500 km, a single maneuver per revolution is sufficient for the navigation and spacecraft errors as introduced in this investigation. Because the NRHO is highly sensitive to perturbations near perilune, navigation errors and maneuver execution errors applied close to the Moon destabilize the orbit. Thus, each stationkeeping maneuver is applied at apolune.

Constraint Targets. Potential targets for x-axis crossing control include position and velocity components as well as perilune passage time and perilune radius. The lowest observed stationkeeping costs and highest rates of success (algorithm robustness) are achieved by targeting a rotating x-velocity equal to the value along the long-horizon (LH) reference trajectory, $v_x = v_{xref}$. The focus on the rotating x-velocity alone mirrors the operational stationkeeping algorithms employed by ARTEMIS and WIND.

Target Location. Finally, the location of the target value v_{xref} is adjusted to search for the best target location along the orbit. Placing the target at the $x - z$ plane crossing near perilune generally results in a slightly lower cost than placing the target near apolune. A more significant influence on the stationkeeping cost, however, is the length of the receding horizon for targeting. With a maneuver placed at apolune, v_x can be targeted a half revolution ahead at the following perilune. If the targeting horizon is extended, however, the cost for each maneuver is significantly reduced. In the current study, a receding horizon of 6.5 revolutions is selected. A single-shooter differential corrector is employed to compute a maneuver to achieve $v_x = v_{xref}$ at the target location. If the corrector is unable to converge, the horizon is reduced to 4.5 revolutions. If further convergence failures are encountered, the horizon is reduced to 2.5 revolutions, then finally to half a revolution to give the targeter the best chance to converge. For x-axis crossing control, the stationkeeping algorithm proceeds as follows:

1. At apolune, employ a differential corrector to target a maneuver that achieves a value $v_x = v_{xref}$ at perilune 6.5 revolutions downstream.
2. If convergence fails, reduce the targeting horizon.
3. Propagate to the next apolune and repeat.

The x-axis crossing control strategy is further detailed in Guzzetti et al.[14]

No optimization process is applied to the maneuver computation in this procedure. Rather, a feasible solution is accomplished by varying the three components of the impulsive Δv. In the operations of both the ARTEMIS and WIND missions, the optimal maneuver direction vector aligned with the stable mode associated with the halo orbit.[3,13,16] This fact led to the reduction of overall stationkeeping Δv without requiring optimization of every maneuver. However, constraining the maneuver direction to align with the stable mode corresponding to the NRHO in the *x*-axis crossing control approach has not delivered an observable reduction in stationkeeping cost. Due to the nearly-linearly stable nature of the NRHO, the stable mode direction is not well defined and, therefore, the stable eigenvector from the NRHO monodromy matrix may not provide useful direction information. Alternatively, the Cauchy-Green Tensor (CGT) is employed to offer dynamical information that leads to optimally oriented maneuvers.

CGT Targeting Stationkeeping can be considered as the use of a maneuver to control downstream position and velocity. In general, stationkeeping processes deliver maneuvers that target a given downstream state, x_T. For a particular fixed-magnitude maneuver, combinations of attainable position and velocity states describe a region that is accessible. However, for some fixed-magnitude maneuvers, x_T may lie outside of the attainable region. In this case, the locally optimal maneuver direction for the given magnitude Δv is the one that guarantees closest proximity to x_T.

For sufficiently small correction maneuvers, such as SH maneuvers, determination of the attainable region geometry is based on an understanding of the evolution of perturbations to a nominal orbit.[17] From this perspective, the dynamical flow nearby a baseline path may be described as the stretching of a fictitious material volume over a given time interval, where the shape of the volume at the final time provides information on the attainable region in the case of a maneuver. The stretching for the material volume is mathematically approximated by the Cauchy-Green Strain Tensor. The CGT, C, is the product of the transpose of the STM with itself,[18]

$$C(t_f, t_0) = \Phi^T(t_f, t_0)\Phi(t_f, t_0) \tag{2}$$

where t_0, and t_f denote the fixed initial and final epochs. The eigendecomposition of the CGT allows identification of the principal directions of expansion for the dynamical flow, including those that are locally associated with the largest and smallest stretching. Note that the CGT is - by definition - a positive definite matrix; it is, therefore, better behaved than the corresponding STM. Note, λ_i and $\boldsymbol{\xi}_i$ are the eigenvalues and eigenvectors of the tensor. Accordingly, within a linear approximation, the local phase space expands or contracts in the direction $\boldsymbol{\xi}_i$ by a factor $\sqrt{\lambda_i}$, as

$$||\Phi(t_f, t_0)\boldsymbol{\xi}_i|| = \sqrt{\lambda_i}||\boldsymbol{\xi}_i|| \tag{3}$$

Within a linear approximation, Eq. (3) describes a continuum that contracts or expands while maintaining an ellipsoidal shape. The principal directions $\boldsymbol{\xi}_i$ may be mapped to the final time as $\Phi(t_f, t_0)\boldsymbol{\xi}_i/||\boldsymbol{\xi}_i||$ to describe the ellipsoid axes; the ellipsoid size along each axis is derived from the rates of expansion and contraction, $\sqrt{\lambda_i}$, as $\sqrt{\lambda_i}||\boldsymbol{\xi}_i||$. The CGT and its eigendecomposition enable an approximation for the attainable region nearby a reference, such as that in the proposed stationkeeping strategy. For CGT targeting, a type of attainable region control, the stationkeeping algorithm proceeds as follows:

1. For a given Δv vector, determine an approximation for the attainable region $\mathcal{E}$ using the CGT.
2. Find the point within the attainable region $x^* \in \mathcal{E}$ that is closest to the target point, x_T.
3. Map the optimal point x^* backward to the initial time to construct the correction maneuver.

Varying the magnitude of the Δv allows for an adjustment of the size of the attainable region.

NRHO ORBIT MAINTENANCE COSTS

With two orbit maintenance schemes defined, the techniques are applied to various NRHOs to assess annual costs for SH stationkeeping maneuvers. A first look is provided by a LinCov analysis applied to x-axis crossing control, and then Monte Carlo trials are run using both x-axis crossing control and CGT targeting. The analyses validate the effectiveness of the two methods and offer insight into the expected annual cost to maintain a habitat spacecraft in an NRHO over long durations.

Navigation and Spacecraft Error Modeling

In the stationkeeping analyses, errors are applied to simulate navigation errors as well as operational noise on the human habitat spacecraft. Several combinations of possible errors are applied to estimate a lower and upper bound on the expected orbit maintenance costs. Three levels of navigation errors on the state are investigated. If the navigation is relatively accurate, a 3σ knowledge error of 1 km in position and 1 cm/s in velocity is assumed. For a mid-level accuracy, a 3σ knowledge error of 10 km and 10 cm/s is applied. A third level, assuming larger navigation errors, is also investigated, with a 3σ error of 100 km and 100 cm/s in position and velocity. The same three error levels are assumed for initial insertion into the halo orbit. The highest level of navigation errors may seem excessive, but it serves to bound the problem for the NRHO regime. The navigation/insertion errors are summarized in Table 1.

Table 1: Three levels of insertion and Navigation Errors

Insertion and navigation errors (zero mean, 3σ)					
Low		Medium		High	
position	velocity	position	velocity	position	velocity
1 km	1 cm/s	10 km	10 cm/s	100 km	100 cm/s

For some simulations, perturbations associated with the spacecraft itself are also included. Thus, two spacecraft configurations are investigated: a quiet spacecraft configuration (no humans present, no attitude deadbanding required) and a noisy spacecraft configuration (humans on board, 3-axis stabilized). The quiet spacecraft configuration incorporates SRP error and maneuver execution errors in addition to navigation errors. The SRP force is modeled assuming a spacecraft mass of 25,848 kg, a nominal spacecraft area of 50 m^2, and a nominal coefficient of reflectivity (C_r) of 2. A 5% error on SRP area (1σ) and a 10% error on coefficient of reflectivity, C_r, (1σ) simulate errors in the SRP calculation. Two maneuver execution error models are investigated: a fixed error model and a percent error model. In the fixed model, a maneuver execution error of 0.03 cm/s is assumed, applied in a random direction. In the percent error model, a 1% error (1σ) is applied to the maneuver magnitude. In all cases, a minimum maneuver threshold of 0.15 cm/s is implemented. If a computed Δv is less than the threshold, it is not executed. The quiet spacecraft errors are summarized in Table 2.

Table 2: Quiet spacecraft configuration

Quiet spacecraft errors		
Maneuver Execution (fixed)	0.03 cm/s	fixed, random direction
Maneuver Execution (percent)	1%	1σ, 0 mean, Gaussian
SRP Area	5%	1σ, 0 mean, Gaussian
C_r	10%	1σ, 0 mean, Gaussian

For a noisy spacecraft inhabited by humans and 3-axis stabilized, additional errors are assumed. The noisy spacecraft errors are included in addition to the navigation errors and quiet spacecraft errors. These errors include mismodeling of attitude deadband and slew maneuvers, as well as CO_2 expulsion (PSA puffs) and urine dumps. At this time, no apriori modeling of the PSA puffs or urine dumps is assumed. The magnitude and frequency of noisy spacecraft errors are summarized in Table 3.

Table 3: Noisy spacecraft configuration

Noisy spacecraft errors. Fixed magnitude, random direction.		
Error Type	*magnitude (m/s)*	*frequency*
PSA Puffs	8.3480E-4	every 10 min
Attitude deadbands	2.0043E-5	every 70 min
Attitude slews	6.9751E-4	every 3.2 hours
Urine dumps	1.8840E-3	every 3.0 hours

The assumptions for the LinCov analysis are consistent with the values in Table 3, but the errors are treated as equivalent process noise acting continuously. In the LinCov analysis, SRP is not modeled in the dynamics but is included as process noise, as summarized in Table 4. The low-level magnitudes of 1 km and 1 cm/s (3σ) are assumed for insertion error (initial dispersion) and navigation error. Finally, maneuver execution error magnitude of 0.03 cm/s (3σ) is also included in the LinCov analysis.

Table 4: Spacecraft process noise for LinCov.

1σ process noise	
Error Type	*per axis value (m^2/s^3)*
SRP	3.0444E-16
Attitude deadbanding	3.1883E-14
Attitude slews	1.4073E-11
Urine dumps	1.0958E-10
PSA puffs	3.7231E-10
Total	1.4073E-11

LinCov: *X*-Axis Crossing Control

Linear covariance analysis is often used early in the mission design cycle for quick assessments before Monte Carlo analysis capability is available. Thus LinCov results are presented prior to the Monte Carlos as a complementary datapoint. The process noise assumptions are included according to Table 4. The LinCov analysis aggregates all quiet and noisy spacecraft errors together in its analysis.

The annual Δv cost from LinCov analysis for the *x*-axis crossing control stationkeeping method is given in Table 5. The particular NRHO evaluated is the r_p = 3233 km 9:2 lunar synodic orbit with an initial epoch of 09 Jan 2020. The contribution to the cost from each error source is given, with the initial dispersion and initial navigation error listed by component in the Moon-centered rotating (MCR) frame. With the exception of the *z*-axis position (out of the Earth-Moon orbit plane), neither the initial dispersions nor the maneuver execution error are significant to the cost. Velocity navigation errors have a larger impact than position navigation errors, with the Δv cost being most sensitive to *x*-axis velocity error in particular. This result is not surprising since the stationkeeping method under study relies on controlling *x*-axis velocity. For a spacecraft inhabited by humans, the Δv cost is dominated by the noise due to slews, urine dumps, and PSA puffs by far. The contribution of each error source is given in Table 5. With all errors in the table included, the total mean annual Δv is 7.79 m/s. The largest portion of this, 6.73 m/s, comes from the errors due to PSA puffs. If PSA puffs were alone eliminated the total cost could be reduced to 3.9 m/s which is practically half the total with PSA puffs present. The most useful result from this analysis is the relative effect of different error sources on the total cost in that it provides impetuous into pursuing techniques that may improve the ability to model the various perturbations from which the LH reference could be adjusted accordingly.

Table 5: Sensitivity of stationkeeping costs to individual errors from LinCov analysis.

	1 km, 1 cm/s, 3σ	
	annual Δv (m/s)	
Error	**mean**	σ
Initial *x* position dispersion	0.00	0.00
Initial *y* position dispersion	0.01	0.01
Initial *z* position dispersion	0.22	0.08
Initial *x* velocity dispersion	0.00	0.00
Initial *y* velocity dispersion	0.00	0.00
Initial *z* velocity dispersion	0.05	0.02
Initial *x* position nav error	0.19	0.05
Initial *y* position nav error	0.19	0.06
Initial *z* position nav error	0.04	0.01
Initial *x* velocity nav error	0.44	0.13
Initial *y* velocity nav error	0.39	0.11
Initial *z* velocity nav error	0.22	0.06
Maneuver execution error	0.02	0.01
SRP	0.01	0.00
Deadbanding	0.06	0.02
Slews	1.31	0.39
Urine dumps	3.65	1.09
PSA puffs	6.73	2.00
Combined total	7.79	2.32

Based on past linear covariance analyses,[19] LinCov results are typically accurate to within a few percent of Monte Carlo results. However, for this problem there are enough differences between the two analysis methods and their implementations that a thorough comparison is beyond the scope of this paper. For example, in the Monte Carlo simulation, a single state is propagated and navigation error is added at each maneuver, whereas in LinCov the covariances for trajectory and navigation dispersions are propagated and updated separately. Another difference is that the Δv imparted from the different disturbances can cancel out in a Monte Carlo run, whereas the corresponding process noise in LinCov is strictly additive since it's applied to the covariance. Moreover, the need to simulate a very long time interval for this problem adds to the difficulty. Thus the LinCov analysis serves to bound results, point out sensitivities, and provide some insight and another point of reference, not take the place of Monte Carlo analysis, presented next.

Monte Carlo: *X*-Axis Crossing Control

A Monte Carlo analysis is executed using x-axis crossing control to investigate expected annual costs for stationkeeping a human orbital habitat in NRHO based on various sets of navigation and spacecraft errors. Navigation and spacecraft errors are applied according to the values in Table 1 to Table 3. Cases are run for both quiet and noisy spacecraft configurations for several reference NRHOs. The force model used for the x-axis crossing control Monte Carlo analysis includes the Sun, Earth, Moon, and Jupiter, whose motions are modeled using the DE430 ephemeris. The Sun, Earth, and Jupiter are modeled as point masses, while the Moon's gravity is modeled using the GRAIL (GRGM660PRIM) model truncated to degree and order 8. The algorithm is implemented in the Commercial Off-the-Shelf (COTS) mission analysis software FreeFlyer™, with integration performed using a Runga-Kutta 8-9 variable step integrator.

The stationkeeping process applied in the x-axis crossing control Monte Carlo analysis is summarized as follows. For each Monte Carlo trial the following steps are implemented:

1. Compute insertion error and apply to position and velocity at spacecraft apolune.
2. Compute error on Cr.
3. Varying the three components of an impulsive maneuver, target $v_x = v_{xref}$ at periapsis 6.5 revs ahead. No errors are included in propagation during targeting.
4. If targeter fails to converge, reduce horizon to 4.5, 2.5, or 0.5 revs ahead, as needed. If targeter still fails to converge, mark case as failed.
5. Compute navigation error and perturb spacecraft position and velocity accordingly.
6. Compute SRP area error; apply Cr error and SRP area error to spacecraft.
7. If the targeted Δv is greater than the minimum threshold, maneuver the spacecraft using the targeted Δv, perturbed by computed maneuver execution error. If the targeted Δv is smaller than the minimum threshold, skip the maneuver.
8. Propagate spacecraft to next apolune. If applicable, compute and apply noisy-spacecraft perturbations in the form of impulsive Δvs at specified intervals.
9. Return to Step 3 and repeat for 50 revolutions.

The Monte Carlo analysis focuses on six reference NRHOs. Each is characterized by its closest approach to the Moon, with perilune distances ranging from 2100 km to 6500 km, as plotted in Figure 2(b). The starting epochs of each reference NRHO are summarized in Table 6. Each Monte Carlo trial is propagated for 50 revolutions, about a year. For each trial, the total stationkeeping Δv is recorded and normalized by the total propagation time to report a value for an annual Δv cost. For each set of trials, the maximum, minimum, and mean annual Δv costs are reported, along with the standard deviation. Cases are run for noisy and quiet spacecraft, each with low, medium, and high navigation errors.

Table 6: Initial epochs for reference NRHOs.

r_p	Epoch	r_p	Epoch
2100	24 Nov 2022 03:07 UTC	5000	12 Jan 2020 02:21 UTC
3233	09 Jan 2020 00:18 UTC	5961	07 Jan 2020 09:01 UTC
4500	01 Jan 2020 01:03 UTC	6500	25 Jan 2020 13:37 UTC

Assuming a quiet spacecraft configuration, the computed stationkeeping costs for the four reference orbits appear in Table 7. Each case is comprised of 500 Monte Carlo trials. As expected, smaller navigation errors lead to lower annual stationkeeping costs. Note that for each category of navigation errors, the mean stationkeeping costs tend to decrease with decreasing perilune distance. For low (1 km, 1 cm/s) navigation errors and medium (10 km, 10 cm/s) navigation errors, the x-axis crossing control stationkeeping method achieves 100% success. For very high (100 km, 100 cm/s) navigation errors, some Monte Carlo trials fail, where a failure is characterized by a spacecraft that escapes the NRHO. The rate of failure with high navigation errors appears in the right-hand column of Table 7. Larger failure rates of 4.3% and 7.4% are observed for the two largest-r_p orbits investigated. It is possible that by updating tuning parameters, an improved rate of success could be achieved for these larger orbits. The application of high sources of navigation error helps bound the performance of the algorithm, but noting a failure does not preclude the ability to target back to the NRHO with a long horizon correction maneuver. However, it does demonstrate the sensitivity of the NRHO regime in the presence of uncharacteristically high navigation errors.

Table 7: Stationkeeping costs for quiet spacecraft

	1 km, 1 cm/s, 3σ				10 km, 10 cm/s, 3σ				100 km, 100 cm/s, 3σ				
	annual Δv (m/s)				annual Δv (m/s)				annual Δv (m/s)				
	max	min	mean	σ	max	min	mean	σ	max	min	mean	σ	failed
r_p = 6500 km	0.30	0.16	0.22	0.06	7.85	1.56	2.38	1.60	67.03	17.24	29.03	16.18	7.4%
r_p = 5931 km	0.29	0.14	0.22	0.05	6.95	1.54	2.29	0.98	181.15	15.28	28.48	33.91	4.3%
r_p = 5000 km	0.30	0.14	0.22	0.06	7.71	1.49	2.25	1.27	194.58	15.22	26.51	29.21	1.6%
r_p = 4500 km	0.29	0.13	0.21	0.06	5.70	1.46	2.13	0.74	231.21	13.79	25.59	33.26	0.6%
r_p = 3233 km	0.27	0.12	0.19	0.05	2.45	1.41	1.88	0.45	49.53	13.64	20.13	7.83	0.6%
r_p = 2100 km	0.28	0.08	0.13	0.06	3.29	1.00	1.47	0.55	45.63	9.01	15.53	11.73	2.8%

The individual stationkeeping maneuvers in each Monte Carlo trial vary; however, certain patterns are apparent. The maneuver magnitudes for 100 Monte Carlo trials of the 9:2 synodic reference ($r_p \approx$3233 km) with low navigation errors appear in Figure 8. The individual maneuvers appear in Figure 8(a). The magnitude of each maneuver remains below 20 mm/s. The sawtooth pattern apparent in the plot suggests that frequently, a maneuver below the minimum threshold (1.5 mm/s) is computed. This suggests that a stationkeeping algorithm that applies a maneuver less frequently, rather than once per revolution, may be effective for an accurately-navigated quiet spacecraft in NRHO. In the current algorithm, skipped maneuvers occur when the targeted maneuver is smaller than the allowed minimum. For the case pictured in Figure 8, the rate of skipped maneuvers is, on average, 26%. The cumulative Δv over time appears in Figure 8(b). The small errors in this case yield few outliers in the cumulative Δv.

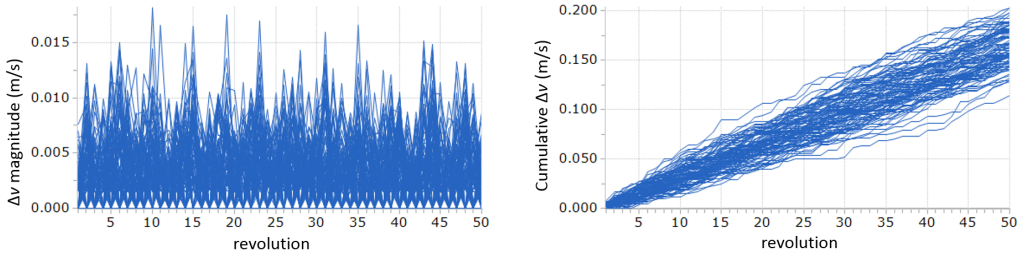

(a) Stationkeeping burn magnitude vs. revolution

(b) Cumulative Δv vs. revolution

Figure 8: Stationkeeping burn magnitude over time for for 100 Monte Carlo trials. 9:2 synodic reference NRHO ($r_p \approx$3233 km), quiet spacecraft, low navigation errors.

When navigation errors are increased, outliers are more apparent in the individual Monte Carlo trials. The maneuver magnitudes vs. time for the 9:2 synodic reference with high navigation errors appear in Figure 9 for 100 Monte Carlo trials. The individual maneuvers in this case can reach magnitudes over 5 m/s, as is apparent in Figure 9(a). While a sawtooth pattern is still visible, the minimum magnitude of the smaller maneuvers is

generally nonzero, and on average, only 0.4% of maneuvers are skipped due to their small magnitude. The cumulative Δv vs. time appears in Figure 9(b) and displays a wide spread of total Δv magnitudes ranging from 10 to 25 m/s for the 100 Monte Carlo trials represented.

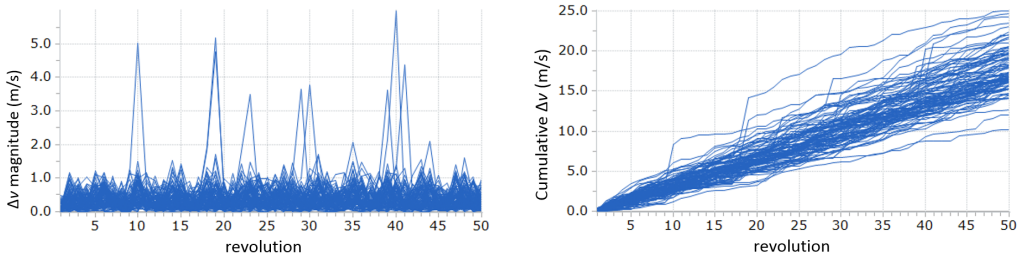

(a) Stationkeeping burn magnitude vs. revolution

(b) Cumulative Δv vs. revolution

Figure 9: Stationkeeping burn magnitude over time for for 100 Monte Carlo trials. 9:2 synodic reference NRHO ($r_p \approx$3233 km), quiet spacecraft, high navigation errors.

The Monte Carlo analysis is repeated with noisy spacecraft assumptions. Each of the four NRHOs is subjected to three levels of navigation errors, and each case is again run for 500 Monte Carlo trials with 50 revolutions per trial. The results of the Monte Carlo analysis appear in Table 8. As with the quiet spacecraft errors, the mean stationkeeping costs tend to decrease with decreasing perilune distance. When navigation errors are small, the costs to maintain the NRHO with noisy spacecraft errors are significantly larger than the cost to maintain the same NRHO with a quiet spacecraft. However, as the navigation errors increase, the differences between the noisy and quiet spacecraft stationkeeping become less pronounced. The noisy spacecraft is only slightly more expensive than the quiet spacecraft for mid-level navigation errors, and the differences are minimal for large navigation errors. As in the quiet spacecraft cases, the x-axis crossing control algorithm yields 100% success for noisy spacecraft stationkeeping with low and mid-level navigation errors. With high navigation errors, however, the failure rate is as high as 8.8% for the 6500 km r_p NRHO. The failure rate values for the high navigation error cases appear in the right hand column of Table 8.

Table 8: Stationkeeping costs for noisy spacecraft

	1 km, 1 cm/s, 3σ				10 km, 10 cm/s, 3σ				100 km, 100 cm/s, 3σ				
	annual Δv (m/s)				annual Δv (m/s)				annual Δv (m/s)				
	max	min	mean	σ	max	min	mean	σ	max	min	mean	σ	failed
r_p = 6500 km	6.92	1.00	1.56	0.98	17.22	1.88	2.78	1.90	145.15	16.82	29.56	26.31	8.8%
r_p = 5931 km	7.82	1.00	1.53	1.10	12.38	1.87	2.81	1.86	140.31	15.98	28.14	28.23	1.6%
r_p = 5000 km	2.02	0.99	1.45	0.36	10.65	1.81	2.71	1.85	154.86	16.02	26.78	42.93	0.6%
r_p = 4500 km	2.02	1.02	1.41	0.36	22.41	1.89	2.66	2.48	221.20	15.72	26.86	42.44	7.0%
r_p = 3233 km	1.69	0.84	1.26	0.30	3.37	1.53	2.26	0.54	51.48	13.27	20.27	8.08	0.0%
r_p = 2100 km	1.79	0.67	1.10	0.35	2.91	1.11	1.83	0.63	60.04	9.67	15.90	13.23	1.4%

The sensitivity of the stationkeeping cost to individual errors is investigated by adding the noisy errors one at a time to the quiet spacecraft setup. A set of 100 Monte Carlo trials is run for the 9:2 synodic reference ($r_p \approx$ 3233 km) with low navigation errors. The results appear in Table 9. The top row represents the quiet spacecraft setup: navigation and maneuver execution errors only. The following 5 rows each represent the quiet spacecraft baseline with a single error type added.

Attitude deadband errors and SRP errors have negligible effects on the annual stationkeeping cost. Errors on the attitude slew modeling has a larger effect, followed by perturbations due to urine dumps. It is noted that these errors could be reduced or eliminated by modeling the acceleration due to the dumps or by assuming the waste is recycled rather than expelled from the spacecraft. The largest source of error on the noisy spacecraft is provided by the PSA puffs due to their frequency (every 10 minutes) where a random direction is assumed. If the puffs occur in a consistent direction and are unmodeled, they can increase stationkeeping cost by an order of magnitude. However, in such a situation the acceleration would be predictable and the

Table 9: Sensitivity of stationkeeping costs to individual errors

	1 km, 1 cm/s, 3σ			
	annual Δv (m/s)			
Included errors	max	min	mean	σ
quiet	0.24	0.13	0.18	0.02
quiet + deadbands	0.23	0.14	0.18	0.02
quiet + SRP	0.25	0.14	0.19	0.02
quiet + slews	0.36	0.20	0.27	0.03
quiet + urine dumps	0.75	0.42	0.60	0.07
quiet + PSA puffs	1.41	0.89	1.13	0.12
quiet + noisy x1	1.69	0.99	1.26	0.13
quiet + noisy x2	3.30	1.80	2.47	0.25

stationkeeping maneuvers could be biased to counteract the effects of the PSA puffs. This result agrees directly with the sensitivity ascertained in the LinCov analysis: PSA puffs are the highest source of error and resultant orbit maintenance cost and thus the out-gassing plan should be considered carefully in the design of any habitat. The final two rows in Table 9 represent the spacecraft with the full set of noisy spacecraft errors; the first is run with noisy errors at their nominal magnitude (noisy x1) and the second at double the magnitude (noisy x2). In this example, doubling the magnitude of the noisy spacecraft errors approximately doubles the orbit maintenance cost.

Monte Carlo: CGT Targeting

A Monte Carlo analysis using CGT Targeting to analyze expected annual costs for stationkeeping a crewed habitat in an NRHO is investigated. For the CGT analysis, errors are applied according quiet spacecraft configuration with low and medium navigation errors given in Tables 1 and 7. The force model includes the Sun, Earth, Moon, and Jupiter modeled as point masses. The process for each Monte Carlo trial using CGT Targeting is summarized as follows:

1. Compute insertion error and apply to position and velocity states at the current spacecraft location.
2. If a maneuver is planned for the current state, apply with the addition of a percent magnitude error. If no maneuver is planned for the current state, or to mimic a missed burn, consider the applied Δv to be zero.
3. Propagate the current state until the next maneuver event and record the state variable vector x_M and epoch, E_M.
4. Select a target from the pre-computed target list to obtain the target state vector and epoch, x_T and E_T, such that $E_T > E_M$.
5. Compute the next maneuver, the correction burn, Δv_M by employing the CGT targeting algorithm.[14]
6. Update the initial state by setting x_M and E_M as the current state vector and epoch, respectively.
7. Return to step 2 and repeat for 45 revolutions.

The Monte Carlo analysis focuses on three reference NRHOs which are characterized by their corresponding CR3BP perilune distances. Each of the 500 Monte Carlo trials is conducted for 45 revolutions to span approximately one year. A targeting horizon of 1 revolution is applied, as compared to a horizon of 6.5 revolutions in the x-axis targeting algorithm. The difference in horizon length accounts for differences in the computed stationkeeping costs between the two algorithms and could likely be normalized if the same assumption was applied to both approaches.

Table 10: Stationkeeping costs for quiet spacecraft using CGT Targeting

	1 km, 1 cm/s, 3σ				10 km, 10 cm/s, 3σ			
	annual Δv (m/s)				annual Δv (m/s)			
	max	min	mean	σ	max	min	mean	σ
r_p = 3500 km	2.80	1.94	2.42	0.12	11.34	6.37	8.38	0.82
r_p = 4600 km	4.98	2.71	3.84	0.46	31.43	10.17	17.14	3.62
r_p = 6000 km	3.38	1.78	2.59	0.28	24.93	7.58	15.39	2.89

NRHO OFF-NOMINAL CORRECTION TECHNIQUES

The analysis is augmented with the inclusion of off-nominal correction techniques. First, missed stationkeeping maneuvers are explored to determine the effects on cost and robustness of the CGT algorithm. Similarly, phase change maneuvers are investigated to assess the costs associated with maneuvering the spacecraft to avoid an eclipse or enable rendezvous.

Missed Burns

Using the CGT targeting stationkeeping method, a scenario where either 5% or 10% of the orbit maintenance burns are missed is considered. For example, for a series of 45 maneuvers and a 10% failure rate, 4-5 maneuvers within the series, on average, deliver no Δv. The results for the Monte Carlo analysis are summarized in Table 11 for a 5% and 10% maneuver failure rates. The results for a nominal (0% failure) analysis are included for reference. For the available trials, the CGT targeting algorithm never fails to sustain the virtual baseline motion when a 5% chance of missing a burn is incorporated. Given a 5% maneuver failure rate, the annualized Δv is, on average, less than 10 m/s for the orbits tested. Increasing the failure rate to 10% drives the annualized Δv to slightly larger values and diminishes the success rate. The maximum Δv total for a series of maneuver among the 500 Monte Carlo trials is one order of magnitude larger than the corresponding average in Table 10.

Table 11: Annual Δv cost for 0%, 5%, and 10% maneuver failure rates. Quiet spacecraft, low navigation errors.

	0% maneuver failure			5% maneuver failure			10% maneuver failure		
	annual Δv (m/s)		Success	annual Δv (m/s)		Success	annual Δv (m/s)		Success
	max	mean	rate (%)	max	mean	rate (%)	max	mean	rate (%)
r_p = 3500 km	2.80	2.42	100	41.63	9.93	100	164.67	13.89	94
r_p = 4600 km	4.98	3.84	100	41.22	5.37	100	93.12	8.80	100
r_p = 6000 km	3.38	2.59	100	16.62	3.46	100	72.21	5.26	98

A maneuver series history offers insight into the increased stationkeeping cost and reduction of successful trials when missed burns are incorporated in the simulated trajectory. Typically, a missed burn is followed by a peak within the Δv profile. This pattern is visible in the sample maneuver history displayed in Figure 10. After the peak, two scenarios are possible: 1) the maneuver size gradually decreases, returning to the vicinity of the average value before the failure event. This case is shown in the profile in Figure 10(a) after the first missed maneuver, which occurs approximately 90 days after the initial epoch. A second scenario is: 2) the individual maneuver size settles on a larger average than the value preceding the peak, as shown in Figure 10(a) after two consecutive missed maneuvers (located approximately 250 days after the initial epoch). From these simple observations, it is reasonable to infer that a larger total Δv for the 45 revolution trajectory and a higher number of unsuccessful trials are more likely to develop when the Δvs fail to return to the average value from before the failure event.

The missed maneuver analysis offers a bounding case for the effects of failed thrusters. In an operational situation, the above scenario would likely be updated to implement a trim maneuver in the case of a missed burn, rather than wait a full week until the next regularly scheduled stationkeeping maneuver. In the case of a large perturbation, to avoid a large total Δv or an SH algorithm failure (i.e., the algorithm is unable to correct the orbit), the reference trajectory could be updated using an LH maneuver. An SH maneuver history may offer guidance to decide if it is necessary to update the current reference path after a missed burn using an LH maneuver or if it is best to continue using SH maneuvers.

Phasing Maneuvers

A trajectory phase is defined as the epoch for a given point along the nominal trajectory. Varying a trajectory phase is equivalent to modifying the epoch for a single point. A phase adjustment may be useful in several scenarios such as avoiding an eclipse or positioning for far-field rendezvous or for any other unforseen operations need. An adjustment (i.e., adjusting the epoch for a specified target state) could be achieved with

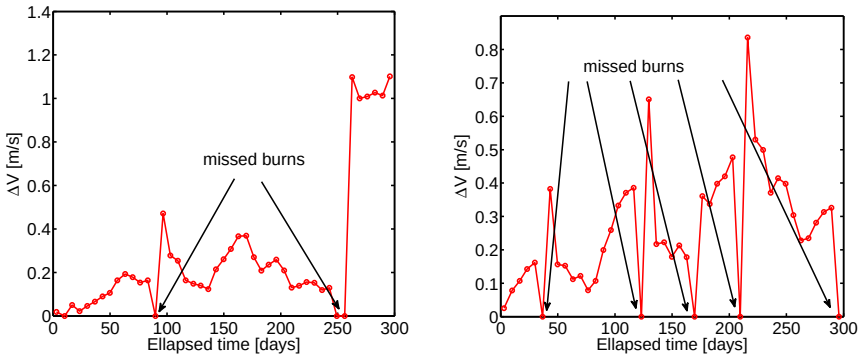

(a) 5% failure rate. (b) 10% failure rate.

Figure 10: Sample SH maneuvers history including missed burns.

an LH maneuver. Along the ephemeris reference orbit, a patch point is created at the target state, and its epoch is constrained to match a desired time that is shifted relative to the original motion. An LH maneuver may be computed using a multiple shooting algorithm.

As a case of study, consider an NRHO with CR3B perilune radius equal to 3500 km. Assume a phasing maneuver is placed at apoasis. This maneuver targets a specified epoch variation for a periapsis some revolutions downstream along the path. To facilitate the convergence of the correction algorithm, both position and velocity for the target point are free to vary. After correction, the target point may no longer be a periapsis. The phase for the periapsis closest to the corrected target is, therefore, verified aposteriori. Note that adjusting the phase for a single patch point alters the phase of other points along the orbit. A particular case is explored to assess the cost of shifting an epoch by a specified number of hours with a variable targeting horizon. The case employs an NRHO with $r_p \approx 3500$ km and a period of about 6.55 days with an initial epoch 23 Nov 2020. The maneuver is placed at apolune to target perilune $n.5$ revolutions downstream. The target is the desired epoch at perilune. An effective representation for the phase difference between two solutions is via the comparison of the time histories of the radial distance from the Moon, as in Figure 11. The phase difference between the original and corrected solution is clear in Figure 11, as the red curve (corrected orbit) is visibly delayed relative to the black curve (nominal motion).

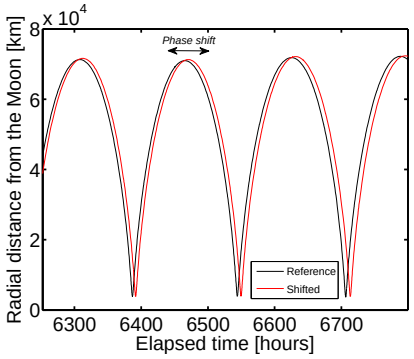

Figure 11: Comparison of a solution phase.

A set of simulations is used to explore different target locations and phase variations. The resulting phasing maneuver Δvs are listed in Table 12 for each combination of target location and phase variation studied. In the table, each row corresponds to a specified time shift for the target, ranging from 1 to 12 hours; each column is a different perilune target. The perilune location is specified as the number of revolutions between the maneuver and the target. From the information available, it appears that the maneuver size decreases if the target is sufficiently distant–in terms of revolutions–from the maneuver location. Also, the Δv cost increases monotonically with the phase shift.

Table 12: Phasing maneuver cost as Δv [m/s] to delay a target periapsis. Point solution analysis.

Epoch shift	Target periapsis			Epoch shift	Target periapsis		
[hrs]	3.5 revs	7.5 revs	11.5 revs	[hrs]	3.5 revs	7.5 revs	11.5 revs
1	2.12	2.80	0.94	-1	2.44	2.98	0.92
2	3.99	5.51	1.87	-2	5.39	6.03	1.77
3	5.50	8.08	2.93	-3	8.80	9.30	2.71
4	6.97	10.58	3.99	-4	12.77	12.56	3.63
5	8.19	13.02	5.16	-5	17.46	15.88	4.55
6	9.15	15.42	6.26	-6	22.57	19.19	5.33
7	9.90	17.73	7.41	-7	27.93	22.33	6.17
8	10.82	19.96	8.58	-8	33.16	25.35	6.97
9	11.69	22.05	9.95	-9	38.21	28.33	7.82
10	12.57	24.23	11.11	-10	42.95	30.96	8.55
11	13.53	26.30	12.36	-11	47.16	33.31	9.23
12	13.93	28.35	13.61	-12	51.06	35.26	9.90

A second example applies a phase shift maneuver to an eclipse avoidance scenario. Eclipses in NRHO occur when the spacecraft passes through the Earth or Moon shadow while crossing the Sun-Earth or Sun-Moon plane. Therefore eclipses are centered on these plane crossings and, thus, are located near perilune. Eclipses by the Earth's shadow can be several hours long and are undesirable from power and thermal considerations.[9] Phasing maneuvers may be introduced to shift the epoch of perilune and avoid an expected eclipse. As an example, consider an NRHO with a starting epoch of 22 Feb 2022 in an approximate 9:2 synodic resonance with $r_p \approx 3233$ km. In a 50 revolution simulation of a quiet spacecraft with low navigation errors, an x-axis crossing control scheme is applied with a targeting horizon of 2.5 revolutions. For a quiet spacecraft with low navigation errors, the stationkeeping Δv history appears in Figure 12(a). Each of the stationkeeping maneuvers remains below 20 mm/s. During the year-long simulation with no phasing maneuvers applied, the trajectory experiences several eclipses from the Moon's shadow and one eclipse from the Earth's shadow. The eclipse history appears in Figure 12(b). The eight blue lines represent Moon shadow events, and the single red line at the 8th revolution identifies the Earth shadow event of concern.

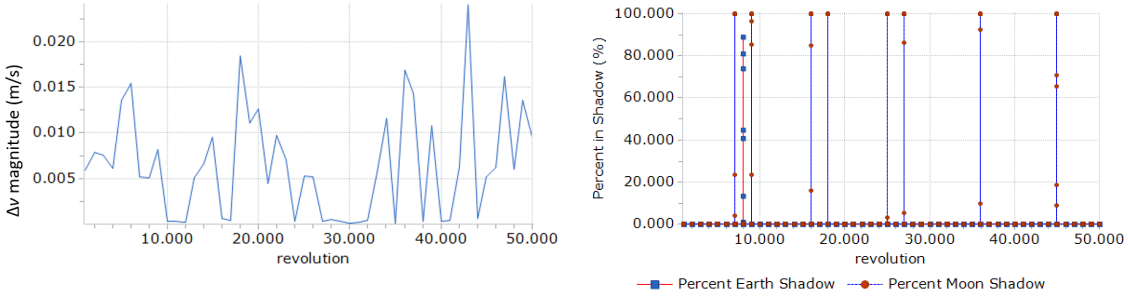

(a) Stationkeeping burn magnitude vs. revolution

(b) Eclipse history vs. revolution

Figure 12: Eclipse history and stationkeeping Δv magnitude over time for an NRHO with $r_p \approx 3233$ km. No phasing maneuver applied.

A phasing maneuver is introduced to shift the epoch of the 8th perilune to avoid the Earth shadow. At apolune on the 6th revolution, the scheduled stationkeeping maneuver is replaced by a phasing maneuver that targets an epoch shift of 3 hours 2.5 revolutions downstream. After the phasing maneuver, the nominal stationkeeping burn schedule is resumed on the 7th revolution with no update to the LH reference. The resulting maneuver history and eclipse history appear in Figure 13. The phasing maneuver magnitude is 2.67 m/s and appears in Figure 13(a) on revolution 6. The maneuver achieves an actual epoch shift of about 1.5 hours at perilune on the 8th revolution. Because no update is made to the LH reference, the post-phasing stationkeeping burn

magnitudes are increased as compared to the nominal case in Figure 13. This increase in stationkeeping Δv after a significant event (in this case, a phasing maneuver) represents a scenario in which the LH reference should be updated to maintain low stationkeeping costs over a long duration. The eclipse history appears in Figure 12(b). The shift in the spacecraft epoch successfully removes the Earth shadow event at the 8th revolution. Downstream, several new Moon shadow events are present, however, no additional Earth shadow events are introduced. The 2.67 m/s phasing maneuver successfully avoids the eclipse due to the Earth's shadow with an epoch shift of 1.5 hours. Note that the computed cost for a 1.5 hour epoch shift at perilune 2.5 revolutions downstream is in line with phasing costs in Table 12.

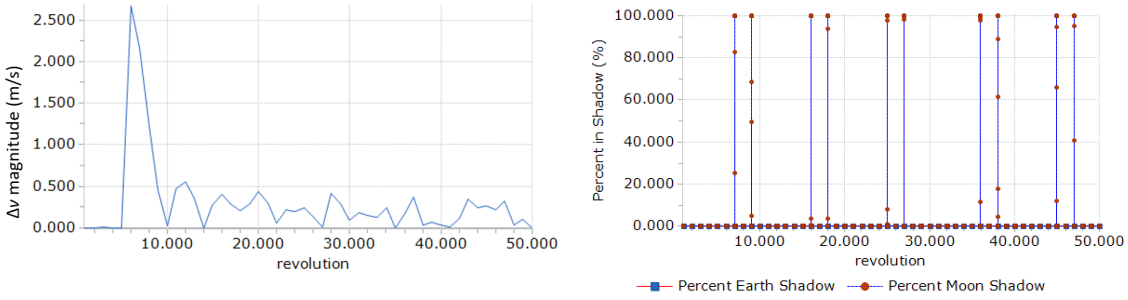

(a) Stationkeeping and phasing burn magnitude vs. revolution

(b) Eclipse history vs. revolution

Figure 13: Eclipse history and stationkeeping Δv magnitude over time for an NRHO with $r_p \approx 3233$ km. Phasing maneuver applied at apolune on the 6th revolution.

NRHO RENDEZVOUS TECHNIQUES AND COSTS

The ability to rendezvous and dock into a fixed location with a preemplaced element will be necessary if assets are to be aggregated at the NRHO. Navigation performance was analyzed for two rendezvous profiles. The first profile begins at a downrange distance from the target of 420 km and 40 km below the target. After five maneuvers (plus a midcourse maneuver), the chaser vehicle arrives at a point 10.7 km downrange and 4 km below the target. Navigation sensors evaluated are the following: An S-band system providing range and range rate measurements potentially beginning at 400 km, an optical camera and IR camera for angular measurements, and a LIDAR providing range and angular measurements during proximity operations. The in-plane relative motion with three-standard deviation (three-sigma) dispersion ellipses is shown in Figure 14. The initial navigation errors and trajectory dispersions are based on a cislunar linear covariance analysis

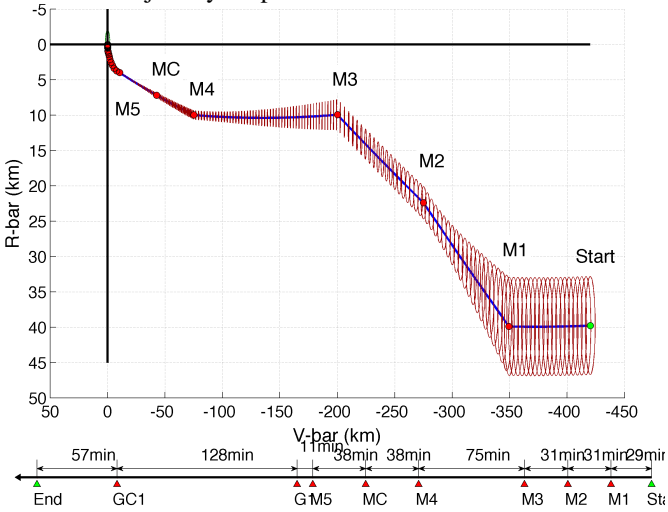

Figure 14: In-plane rendezvous trajectory with three-sigma dispersion ellipses

available from the Orion spacecraft team. The nominal delta-velocity (Δv) to complete this rendezvous profile is 56.3 m/sec.

The cost in Δv actually varies slightly depending on the portion of the NRHO in which the rendezvous occurs. The Δv may exceed 200 m/sec if the rendezvous were to occur very close to perilune. This cost may be reduced somewhat by appropriate adjustments to targeting, but we do not expect that a rendezvous would ever occur very close to perilune in any case. Figure 15 shows a graph of the Δv required as a function of the position in the NRHO. The large peaks all occur at perilune passage.

The second rendezvous profile that was analyzed was developed specifically to reduce the Δv required. If

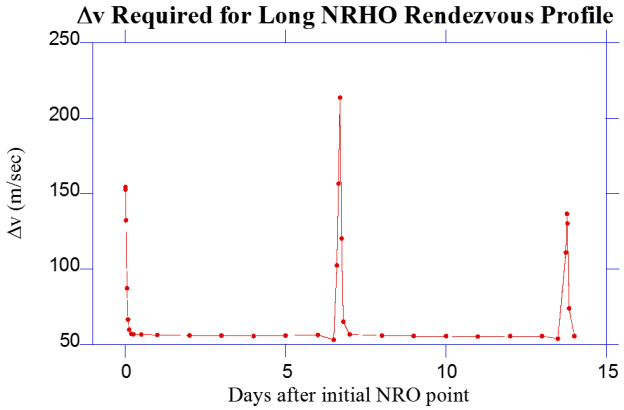

Figure 15: Δv required for rendezvous as function of position with an NRHO

the initial downrange position is shortened from 420 km to about 220 km, the initial downrange velocity may be reduced by a factor of two. This results in less Δv expenditure. Also, reduction of the initial delta-height (ΔH) to 10 km causes a reduction in Δv, and fewer maneuvers are required. The portion of the rendezvous within 10.7 km in downrange distance is identical to the longer profile. The in-plane relative motion for this rendezvous profile is shown in Figure 16.

Navigation analysis of this profile indicates that the accuracy of the sensors required to accomplish the rendezvous is better than for the longer profile. Also, the profile should be lengthened by about 25 min, beginning at about 252 km in downrange distance to allow adequate tracking before the first maneuver. This does not affect nominal Δv cost.

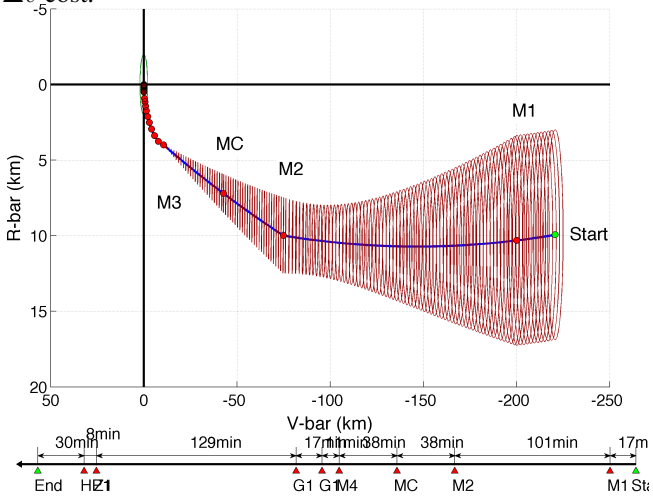

Figure 16: In-plane relative motion for profile beginning at (220,10) km

CONCLUSION

The Near-Rectilinear Halo Orbit regime is of great interest for human spaceflight due to its ability to facilitate missions to multiple destinations: the lunar surface, Mars and beyond. While human spacecraft have not performed missions to orbits of these types, robotic spacecraft have. In this paper, the differences between robotic and human spacecraft needs have been addressed, and the ability to conduct human missions to quasi-stable libration point orbits has been successfully demonstrated. With feasibility studies complete, further refined analysis will aid in assessing the total spacecraft costs for long term operations for a given spacecraft design and navigation strategy.

ACKNOWLEDGMENTS

The authors wish to thank Roland Martinez and Chris D'Souza for their support of this work, which was partially funded by NASA JSC through contract #NNJ13HA01C and grant #NNX13AK60A.

REFERENCES

[1] R. Whitley and R. Martinez, "Options for Staging Orbits in Cislunar Space," *IEEE Aerospace 2015*, Mar. 2015.

[2] D. Cosgrove, B. Owens, J. Marchese, and M. Bester, "ARTEMIS Operations from Earth-Moon Libration Orbits to Stable Lunar Orbits," *Proceedings AIAA SpaceOps Conference*, 2012.

[3] D. Folta, T. Pavlak, A. Haapala, and K. Howell, "Preliminary Design Considerations for Access and Operations in Earth-Moon L_1/L_2 Orbits," *23rd AAS/AIAA Space Flight Mechanics Meeting*, Feb. 2013.

[4] J. Breakwell and J. Brown, "The 'Halo' Family of 3-Dimensional Periodic Orbits in the Earth-Moon Restricted 3-Body Problem," *Celestial Mechanics*, Vol. 20, Nov. 1979, pp. 389–404.

[5] K. Howell and J. Breakwell, "Almost Rectilinear Halo Orbits," *20th Aerospace Sciences Meeting*, 1982.

[6] D. Grebow, D. Ozimek, K. Howell, and D. Folta, "Multibody Orbit Architectures for Lunar South Pole Coverage," *Journal of Spacecraft and Rockets*, Vol. 45, Mar. 2008.

[7] D. Grebow, D. Ozimek, and K. Howell, "Design of Optimal Low-Thrust Lunar Pole-Sitter Missions," *The Journal of of the Astronautical Sciences*, Vol. 58, Jan. 2011.

[8] D. Folta, M. Woodard, and D. Cosgrove, "Stationkeeping of the First Earth-Moon Libration Orbiters: The ARTEMIS Mission," *AAS/AIAA Astrodynamics Specialist Conference*, 2011.

[9] J. Williams, D. E. Lee, R. L. Whitley, K. A. Bokelmann, D. C. Davis, and C. F. Berry, "Targeting Cislunar Near Rectilinear Halo Orbits for Human Space Exploration," *27th AAS/AIAA Space Flight Mechanics Meeting*, Feb. 2017.

[10] R. Zanetti and C. D'Souza, "Navigation and Dispersion Analysis of the First Orion Exploration Mission," *AAS/AIAA Astrodynamics Specialist Conference*, Aug. 2015.

[11] J. Jang, S. Bhatt, M. Fritz, D. Woffinden, D. May, E. Braden, and M. Hannan, "Linear Covariance Analysis for a Lunar Lander," *AIAA Science and Technology Forum and Exposition*, Jan. 2017.

[12] D. Geller, "Linear Covariance Techniques for Orbital Rendezvous Analysis and Autonomous Onboard Mission Planning," *Journal of Guidance, Control, and Dynamics*, Vol. 29, 2006.

[13] D. Folta, T. Pavlak, K. Howell, M. Woodard, and D. Woodfork, "Stationkeeping of Lissajous Trajectories in the Earth-Moon System with Applications to ARTEMIS," *20th AAS/AIAA Space Flight Mechanics Meeting*, Feb. 2010.

[14] D. Guzzetti, E. Zimovan, K. Howell, and D. Davis, "Stationkeeping Methodologies for Spacecraft in Lunar Near Rectilinear Halo Orbits," *27th AAS/AIAA Space Flight Mechanics Meeting*, Feb. 2017.

[15] G. Wawrzyniak and K. Howell, "An Adaptive, Receding-Horizon Guidance Strategy for Solar Sail Trajectories," *AIAA/AAS Astrodynamics Specialist Conference*, 2012.

[16] J. Petersen and J. Brown, "Applying Dynamical Systems Theory to Optimize Libration Point Orbit Stationkeeping Maneuvers for WIND," *AAS/AIAA Astrodynamics Specialists Conference*, Aug. 2014.

[17] C. Short, *Flow-informed Strategies for Trajectory Design and Analysis*. Ph.D. Dissertation, School of Aeronautics and Astronautics, Purdue University, West Lafayette, Indiana, May 2016.

[18] D. Smith, *An Introduction to Continuum Mechanics after Truesdell and Noll*. Dordrecht: Kluwer, 1993.

[19] R. Zanetti, D. Woffinden, and A. Sievers, "Multiple Event Triggers in Linear Covariance Analysis for Spacecraft Rendezvous," *Journal of Guidance, Control, and Dynamics*, Vol. 35, 2012.